Progress in Additive Manufacturing (2019) 4:13–21
https://doi.org/10.1007/s40964-018-0054-2

FULL RESEARCH ARTICLE

Additively manufactured mixed potential electrochemical sensors for NO_x, C_3H_8, and NH_3 detection

Lok-kun Tsui[1] · Angelica Benavidez[1] · Lindsey Evans[2] · Fernando H. Garzon[1,2]

Received: 26 March 2018 / Accepted: 25 May 2018 / Published online: 1 June 2018

Abstract
Additive manufacturing of mixed potential electrochemical sensors opens the possibility to perform rapid prototyping of electrode and electrolyte materials. We report for the first time the use of this technique for the fabrication of solid-state electrochemical gas sensors of the mixed potential type and assessment of variability in the manufacturing process. $La_{0.87}Sr_{0.13}CrO_3$ (LSCO) and Pt electrodes bridged with a porous yttria-stabilized zirconia (YSZ) have been deposited on YSZ substrates by direct-write extrusion of pastes and inks. The sensors are evaluated for their sensitivity to 200 ppm of NO_x, C_3H_8, and NH_3. There is a need to understand how variations in intrinsic materials parameters during manufacturing such as differences in porosity affect the gas sensing of additively manufactured sensors to guide optimization of their performance and serve as quality control techniques. Further characterizations of these devices include electrochemical impedance spectroscopy and an aqueous electrochemical assessment of the electrode surface area and diffusion through the porous layer. We find a correlation of increased sensitivity with larger gas reaction impedance, higher Pt electrode surface area, and slower diffusion.

Keywords Mixed potential sensor · Yttria-stabilized zirconia · Gas sensor · Extrusion printing

1 Introduction

A major advantage of additive manufacturing (AM) is the capability of producing devices and components at small prototyping scales with a short turnaround time so that materials and processes can be quickly evaluated. Considerable advances have been made with the AM of ceramic materials in a diverse set of applications including passive structural components, transducer devices, and dielectric materials [1–4]. In the direct-write deposition of ceramics called "Robocasting" a slurry containing ceramic particles is extruded from a computer controlled printer to form a desired structure, dried, and then sintered [5]. The additive manufacturing of metal components has also been demonstrated for biomedical, [6, 7] mechanical, [8] and electronics applications [9]. A variety of techniques are available including powder bed fusion, extrusion, and jetting of the material [8, 10]. A number of groups have used AM in the context of sensors to deposit organic or polymer components for sensing volatile organics, [11] charged molecules and surfactants, [12] and H_2S [13]. However, the additive manufacturing of ceramic components for mixed potential sensors is an area which has not been previously investigated.

Mixed potential sensors consist of two dissimilar electrodes bridged by a solid-state electrolyte. The operating principle of a mixed potential sensor is the establishment of a difference in the mixed potential at each electrode due to the differences in catalytic activity towards oxidation and reduction of species in the gas stream [14, 15]. Mixed potential sensors are a promising technology for pollution monitoring because of their demonstrated durability in exhaust gas environments, rapid response time, and tunable selectivity to various gases of interest including NO_x (NO_2 or NO), hydrocarbons, CO, and NH_3 [16–18]. The selection of materials is key to targeting the selectivity of the devices; for example, NO_x and hydrocarbons are most readily sensed

Electronic supplementary material The online version of this article (https://doi.org/10.1007/s40964-018-0054-2) contains supplementary material, which is available to authorized users.

✉ Lok-kun Tsui
lktsui@unm.edu

[1] Center for Micro-Engineered Materials, University of New Mexico, 1001 University Blvd SE, Albuquerque, NM 87106, USA

[2] Advanced Materials Laboratory, Sandia National Laboratories, 1001 University Blvd SE, Albuquerque, NM 87106, USA

by $La_{0.87}Sr_{0.13}CrO_3$ (LSCO)/Pt electrodes while Au and Au alloy electrodes are most selective towards CO [16, 19–21]. Three-electrode devices have been demonstrated for use in the detection and quantification of EPA regulated automotive exhaust gases in sensors with a planar geometry similar to commercially available lambda O_2 sensors [17, 22]. These devices were produced with a screen printing technique that scales well for mass production, but the materials waste for precious metals like Pt, the additional effort needed to create screen printing patterns for each new sensor geometry, and the turnaround time of this process makes this process sub-optimal for rapidly prototyping small numbers of devices. In principle, additive manufacturing substantially decreases both cost and time for rapidly prototyping of custom sensors with a variety of monitoring and feedback control applications.

Variability in the performance of sensors may arise due to inconsistencies across the extrusion process and heat treatment process of each device. There is a need to develop an understanding of how materials parameters including the diffusivity through the porous electrode and the roughness of the electrodes affect the performance of the mixed potential sensors. Aqueous electrochemical tests can easily detect differences in electrode surface area and diffusivity in commercially screen printed and additively manufactured sensor devices. Double layer capacitance is used to measure the surface area of Pt electrodes and the diffusion of ferri/ferrocyanide species is used as a probe for differences in diffusion through the porous layer [23]. In this paper, we report on the manufacturing of LSCO/YSZ/Pt sensors by direct-write deposition of electrode components on a laminated substrate of YSZ. The sensitivity to NO_x, C_3H_8, and NH_3 and its variability were assessed and correlated with impedance spectroscopy, Pt electrode surface area, and diffusivity through the YSZ electrode.

2 Experimental section

2.1 Fabrication of mixed potential sensors

Mixed potential sensor electrodes and electrolytes were deposited on a laminated substrate of green YSZ (3 mol% Y_2O_3) tape (ESL 42000) using a computer controlled extrusion system. The Pt electrodes and leads were deposited as an ink (ESL 5570). The ink was extruded through a nozzle with a 125 µm tip at a table speed of 2 mm/s. The substrate and Pt were co-fired at 1450 °C. The LSCO electrode was deposited as a paste of LSCO powder (Praxair) suspended in a vehicle and thinner (ESL 473 and 401). The LSCO paste was 65 wt% solids and had a vehicle:thinner ratio of 4:1. The LSCO powder, vehicle, and thinner were mixed in a Thinky planetary centrifugal vacuum mixer at 2000 rpm and 85 kPa for 1 min. The paste was then 3-roll milled to break up any agglomerates. The paste was extruded through a nozzle with a 125 µm tip at a table speed of 3 mm/sec. The LSCO electrode was then sintered at 1200 °C. Finally, the porous YSZ electrolyte was formed by extrusion of a YSZ (Tosoh, TZ-3YS) paste. The YSZ paste was 65 wt% solids, had a vehicle:thinner of 4:1, and was processed in the same manner as the LSCO paste. The YSZ paste was extruded using the same parameters as the LSCO paste and was then sintered at 1100 °C. Sintering schedules are available in the Electronic Supplementary Information, Table S1. A schematic and photograph of a sensor are shown in Fig. 1. Ten devices were constructed on a single substrate and sectioned with a diamond wafer cutting saw. Device performance is also compared with a commercially prepared 3-electrode LSCO/AuPd/Pt sensor from ESL ElectroScience.

2.2 Gas sensitivity tests of sensors

The sensors were mounted on a holder obtained from a commercial Bosch Lambda O_2 automotive sensor unit and contacts were made by pressing Ni wires against the Pt contact leads. The wires were passed through an alumina tube and the device was placed in the center of a 1″ quartz tube within a Lindberg Blue tube furnace. Each sensor was heated to a temperature of 500 °C and allowed to remain there for at least 1 h prior to testing. Gas mixing and delivery were provided by an Environics 2000 gas mixer controlled with LabVIEW. The sensors were exposed to a base gas mixture containing 10% O_2 and 2.5% CO_2 with balance N_2 at a flow rate of 180 SCCM. Test gases of 200 ppm of NO, NO_2, C_3H_8, and NH_3 were then introduced into the gas stream. The measurement started with a 30-min stabilization period under base gas, and each test gas was introduced in 10-min intervals, followed by a 10-min purge with base gas. Voltages were recorded between the electrodes using a Keithley 2400 digital sourcemeter under open circuit conditions or with an applied bias of −5.0 µA. The polarity convention used is LSCO as the positive electrode and Pt as the negative electrode.

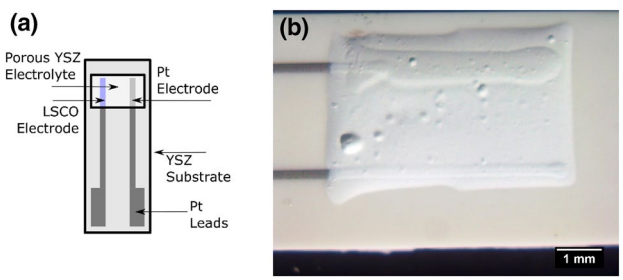

Fig. 1 **a** A schematic of the two electrode LSCO/YSZ/Pt device and **b** a photograph of the sensing element of a completed device

2.3 Other electrochemical testing of sensors

Electrochemical impedance spectroscopy (EIS) and cyclic voltammetry (CV) were performed using a PAR 2273 potentiostat in two-electrode configuration with the LSCO as working electrode and Pt as the counter and reference electrode. CVs were obtained between ±0.3 V at a scanrate of 25 mV/s. EIS was performed with a 10 mV perturbation and frequency range from 100 mHz to 2 MHz. The EIS data were fit to the equivalent circuit model shown in Fig. 2. Impedance measurements were acquired in base gas mixtures and each of the test gas mixtures at 500 °C. One sample was also tested at temperatures between 300 and 525 °C and fit using a modified form of the impedance model where the C2 capacitor is replaced with a constant phase element. The resistance of R2 was converted to conductivity using a rectangular channel geometry. The relationships between the conductivity (σ), Boltzmann's constant (k), absolute temperature (T), an empirical pre-exponential constant (A), and the activation energy (E_a) are given in Eq. 1 [24]. The rearrangement of Eq. 1 into logarithmic form in Eq. 2 can be used to extract the activation energy from the slope of an $\ln(\sigma \times T)$ plot vs. reciprocal temperature.

$$\sigma = \frac{A}{T} \exp\left(-\frac{E_a}{kT}\right) \tag{1}$$

$$\ln(\sigma \times T) = \ln(A) - \frac{E_a}{k}\left(\frac{1}{T}\right) \tag{2}$$

Aqueous electrochemical tests were performed after all gas sensing experiments were completed to ensure no contamination by these experiments. The sensors were prepared by first contacting Ni wires to the Pt electrode of the sensor using an Ag conductive epoxy (Creative Materials 251) and insulating the sample with at least four coats of clear nail polish so that only the Pt electrode and the YSZ on top is exposed to the solution. Electrochemical measurements were taken in a three-electrode configuration with the PAR 2273, a Pt coil counter electrode, and an Ag/AgCl (saturated KCl) reference electrode. The sensors were tested first in a solution of 100 mM H_2SO_4 to obtain the double layer capacitance of the Pt electrodes. A set of 20 CVs were collected between −0.25 and 1.0 V vs. Ag/AgCl to clean the surface and then 20 CVs were collected at varying scan rates between 0.5 and 0.7 V vs. Ag/AgCl and 50–300 mV/s. The double layer capacitance is given by Eq. 3 where I is the current, C_{DL} is the double layer capacitance, and ν is the scanrate.

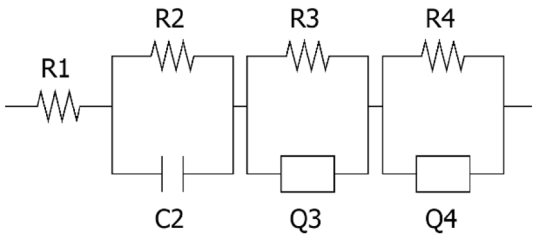

Fig. 2 Electrochemical impedance spectroscopy equivalent circuit model used to fit the impedance data collected on the printed sensors. R represents a resistor, C represents a capacitor, and Q represents a constant phase element

$$I = C_{DL}\nu \tag{3}$$

The double layer capacitance of Pt with a conversion factor [25] of 20 μF/cm^2 was used to assess a roughness factor, the ratio between the real surface area and the geometric surface area. The sensors were then cleaned with DI water, and placed in a solution of 100 mM $K_3Fe(CN)_6$, 100 mM $K_4Fe(CN)_6$, and 1M Na_2SO_4. 20 scans were collected with a potential window between −0.25 and 0.75 V vs. Ag/AgCl at scan rates between 50 and 300 mV/s. The peak in oxidation and reduction of the ferri/ferro-cyanide species were fit to the Randles–Sevcik equation (Eq. 4) [26] to obtain the effective diffusion coefficient through the porous layer.

$$j_p = 2.68\ x\ 10^5\ n^{\frac{3}{2}} D^{\frac{1}{2}} C \nu^{\frac{1}{2}} \tag{4}$$

In Eq. 2, n is the number of electrons transferred, D is the diffusion coefficient, C is the concentration of the redox species in solution, and ν is the scanrate.

3 Results and discussion

3.1 Distribution of sensor response

Figure 3 shows a plot of the distribution of sensor signals for the ten sensors. While the polarity of the measured signals are consistent with LSCO/Pt devices we have previously studied, the signals observed are weaker by a factor of 2–5× compared with the commercially prepared ESL devices such as the 3-electrode LSCO/AuPd/Pt device [17]. The sensors under current bias also show neither the enhancement of NO_x sensitivity nor the suppression of C_3H_8 sensitivity. Furthermore, there is a broad distribution in the responses with the NO_2 test producing a response between 5 and 15 mV response and NH_3 signals spanning −10 to +10 mV.

3.2 Electrochemical impedance spectroscopy

To gain insight into the difference between the ESL sensors and our manufactured devices as well as study the influence of impedance on sensitivity, electrochemical impedance spectroscopy and cyclic voltammetry were performed. Figure 4 shows the impedance spectra taken on one of the

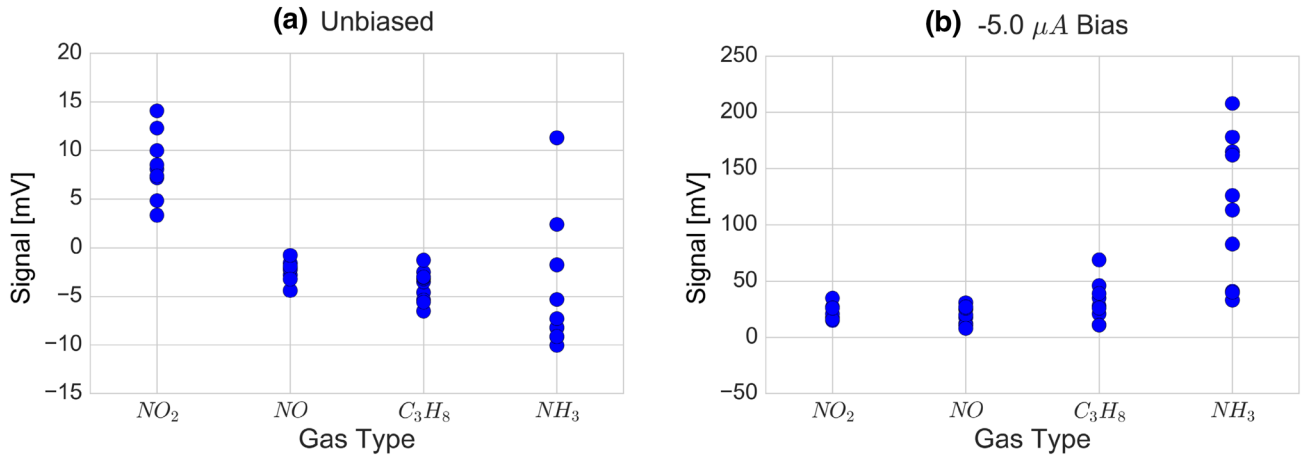

Fig. 3 The distribution of sensor signals in **a** unbiased mode and **b** under a −5.0 muA bias. Signals are approximately 2–5× smaller than planar ESL sensors

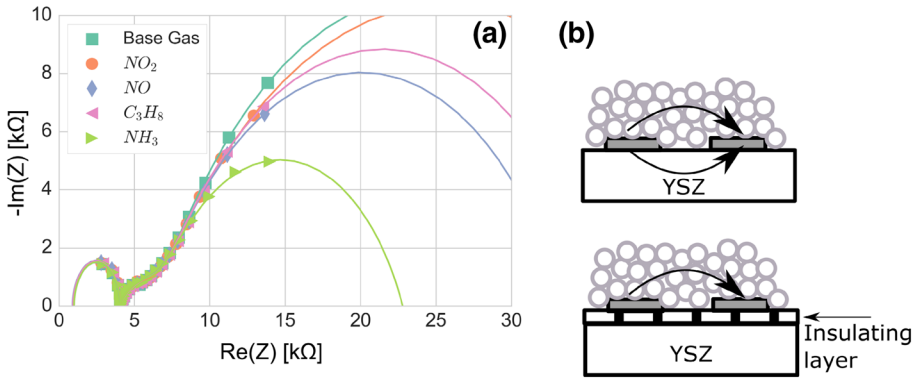

Fig. 4 **a** Impedance spectra of an additively manufactured sensor and **b** a schematic showing potential conduction paths in the absence of (top) and in the presence of (bottom) an insulating layer between the electrodes and the YSZ substrate. In the former, oxygen ions can conduct through both the substrate and the top porous layer. In the latter, only transport through the top porous layer is permitted

sensor samples. There are three time constants observed: a semicircular arc at high frequency situated between 1 and 5 kΩ, a depressed arc at intermediate frequency between 5 and 7 kΩ, and a large depressed arc at low frequency. In comparison to the impedance taken on ESL's sensor (Supplementary Information, Fig. S1), the impedance of our printed devices is an order of magnitude smaller. A key difference between the printed sensors and ESL's devices is the presence of an insulating Mg–Al–O spinel beneath the electrodes which blocks the transport of oxygen ions through the substrate as illustrated in Fig. 4b. The impact of the higher conductivity is found in the CV measurements shown in Supplementary Information, Fig. S2 where under the same applied bias, an increase in current by a factor of 20× is observed in our printed sensors. The current enhancement by introduction of NO_x is only on the order of 0.1–0.3 μA and results in poor signal to noise ratio under bias in the absence of the insulating layer. We also observe an Ohmic resistance absent in the ESL sensors since the intercept of the high frequency arc with the real axis by approximately 1 kΩ. This may indicate a smaller particle size of the Pt contributing a greater grain boundary resistance.

The physical interpretation of the electrochemical impedance analysis is constructed from the equivalent circuit model in Fig. 2. Table 1 shows the results of fitting the same equivalent circuit model to all ten manufactured sensors in base gas and with the addition of 200 ppm of each test gas. The R2/C2 and R3/Q3 elements are not affected by the selection of gases, so these are likely to be associated with ionic transport through the YSZ electrolyte. R4/Q4, however, decreases in the presence of test gas and is smallest in the presence of NH_3. The R4/Q4 equivalent circuit elements are assigned to the impedance associated with electrochemical reactions in the gas phase. The R2/C2 circuit element contains the smallest variability and is smaller on average in magnitude than R3/C3. The R2/C2 and R3/C3 elements are associated with the conduction through the substrate and the porous YSZ electrolyte, respectively, since a smaller resistance is expected for transport through a dense structure compared with a porous one. Measurements of the resistance of the R2 element were performed over a temperature range of 300–525 °C, and the conductivity was plotted in Fig. 5. The conversion from resistance to conductivity was performed by approximating a rectangular channel formed by the two

Table 1 Summary of parameters (minimum, maximum, average, and standard deviation) obtained by fitting the equivalent circuit in Fig. 1 to impedance spectroscopy on the sensors

Test condition	Parameter	Min	Max	Average	Standard deviation
Base gas (10% O_2 + balance N_2)	R1 (Ω)	9.25×10^{2}	1.10×10^{3}	1.02×10^{3}	4.86×10^{1}
	C2 (F)	1.05×10^{-10}	1.22×10^{-10}	1.15×10^{-10}	5.60×10^{-12}
	R2 (Ω)	2.79×10^{2}	4.00×10^{3}	3.07×10^{3}	3.34×10^{2}
	Q3 (F $s^{(\alpha-1)}$)	1.26×10^{-5}	4.86×10^{-5}	2.64×10^{-5}	1.16×10^{-5}
	α3	4.31×10^{-1}	6.50×10^{-1}	5.46×10^{-1}	5.89×10^{-2}
	R3 (Ω)	1.93×10^{3}	8.78×10^{3}	3.59×10^{3}	1.89×10^{3}
	Q4 (F $s^{(\alpha-1)}$)	8.40×10^{-5}	1.56×10^{-4}	1.27×10^{-4}	1.84×10^{-6}
	α4	5.60×10^{-1}	7.97×10^{1}	6.92×10^{1}	6.72×10^{-2}
	R4 (Ω)	2.37×10^{4}	2.41×10^{5}	6.81×10^{4}	6.35×10^{4}
+ 200 ppm NO_2	R4 (Ω)	3.02×10^{4}	1.94×10^{5}	6.75×10^{4}	4.96×10^{4}
+ 200 ppm NO	R4 (Ω)	2.11×10^{4}	8.61×10^{4}	4.12×10^{4}	2.38×10^{4}
+ 200 ppm C_3H_8	R4 (Ω)	2.37×10^{4}	9.40×10^{4}	4.42×10^{4}	2.62×10^{4}
+ 200 ppm NH_3	R4 (Ω)	1.03×10^{4}	3.27×10^{4}	1.78×10^{4}	6.35×10^{3}

R resistance, *C* capacitance, *Q* CPE magnitude, *α* CPE non-ideality parameter

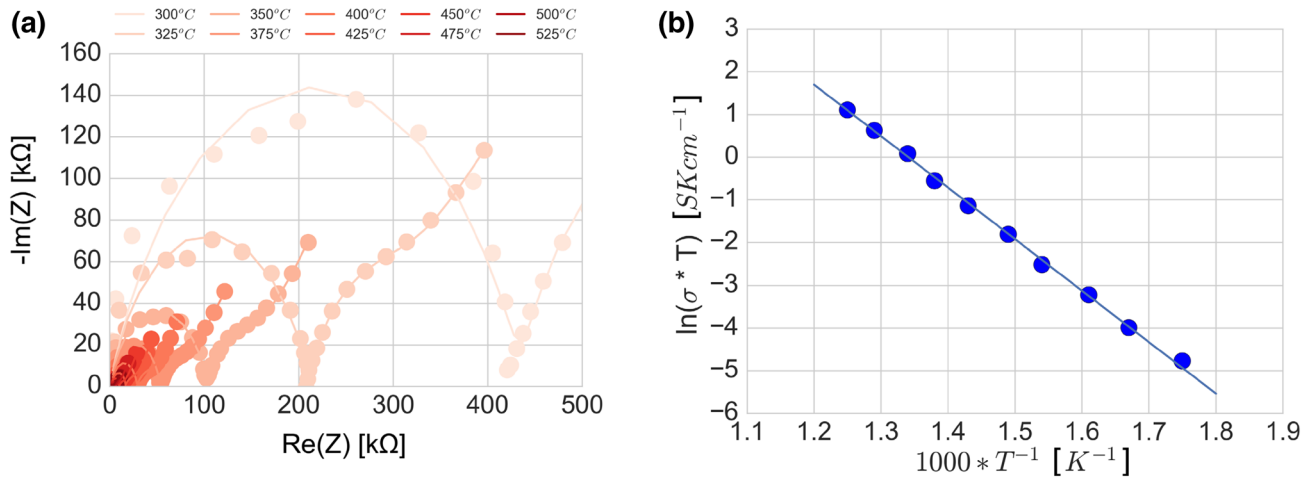

Fig. 5 **a** Impedance spectra collected on a printed sensor at temperatures from 300 to 525 °C. **b** The natural log of conductivity associated with R2 is plotted with respect to reciprocal temperature

Pt contact leads. The slope of the line ($R^2 > 0.999$) in Fig. 5b yields an activation energy of 1.04 eV. This value is close to the value reported by Tuller (0.93 eV) for polycrystalline YSZ and is in support of the assignment of the R2/C2 circuit element with conduction through the substrate [27].

The signal strength for each test gas as a function of the R4 resistance in base gas is plotted in Fig. 6. As the R4 resistance increases, the magnitude of the signal also increases. This indicates that the impedance of this circuit element can be used as a quality control parameter for the signal response of additively manufactured sensors.

3.3 Diffusion through the porous electrolyte

While impedance can be readily measured and used as a quality control parameter, an underlying physical reason for the difference in the signal response of our sensors is sought. Aqueous electrochemical measurements were used to assess the Pt electrode surface area by double layer capacitance and the effective diffusion coefficient by obtaining CVs in a solution of 100 mM $K_3Fe(CN)_6$, 100 mM $K_4Fe(CN)_6$, and 1 M Na_2SO_4. Typical sets of cyclic voltammograms for scan rates from 50 to 300 mV/s and the fit to the Randles–Sevcik equation (Eq. 4) are provided in Fig. S3 in the Supplementary Information. The effective diffusion coefficient varies from 10^{-8} to 10^{-10} cm^2/s, though this level of variability is also observed in screen printed devices [23]. The effective roughness factor determined by the double layer capacitance technique in 0.1 M H_2SO_4 for the Pt exposed through the YSZ varies from 5 to 65, and indicates either that the Pt does not sinter uniformly across these samples or there is a variation in the amount of Pt exposed beneath the YSZ.

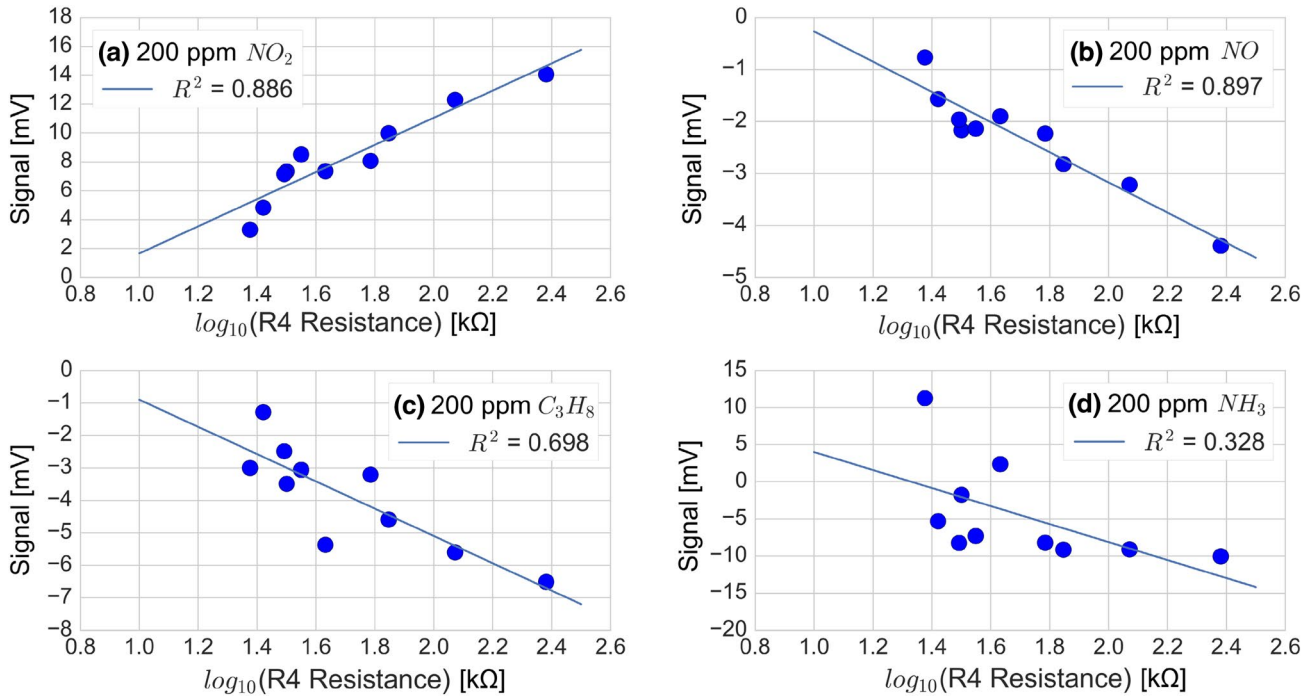

Fig. 6 The sensor response to 200 ppm of **a** NO_2, **b** NO, **c** C_3H_8, **d** NH_3 is found to be linearly correlated with the log of the R4 resistance in base gas. R^2 represents the goodness of fit parameter for a linear fit through the data

Figure 7 shows the correlation of signal response to (a–d) the effective diffusion coefficient, and (e–g) the Pt electrode roughness. The signal associated with NO_x and C_3H_8 are found to be positively correlated to lower diffusion coefficient and lower Pt surface area, while the NH_3 signal is unaffected by these two parameters.

The increased roughness factor of Pt could result in greater heterogeneous catalysis of the gas species, for example, decomposing C_3H_8 into the more easily oxidized CO, which then readily undergo electrochemical reactions at the three-phase interface. Similarly, a more tortuous path through YSZ increases the contact time with the electrolyte, resulting in a higher amount of heterogeneous reactions on the electrolyte prior to reaching the three-phase interface. An alternate explanation for the dependence of the signal on the effective diffusion coefficient is illustrated schematically in Fig. 8, shown for the case of an oxidized gas like C_3H_8. The concentration of test gas species is 1000× smaller than the O_2 concentration in the gas stream, and the electrochemical reaction is expected to be diffusion limited [15]. We assume the oxygen reduction reaction is never diffusion limited and the electrochemical kinetics for Pt are more facile than they are on LSCO. Consider the case of an oxidized gas such as C_3H_8, where three distinct regions appear in Fig. 8. In the limit of high diffusivity indicated by (a), neither electrode is diffusion limited nor the mixed potentials of both electrodes are determined entirely by the electrochemical kinetics. In regions indicated by (b–e) the LSCO electrode is under kinetic control, while the Pt electrode's mixed potential is determined by the intersection of the diffusion limiting current of the oxidized gas with the oxygen reduction reaction current. Within this region the magnitude of the difference in mixed potential between the two electrodes increases. Finally, in the region noted by (f), the mixed potential of both electrodes is controlled by diffusion, and the difference in mixed potential tends towards zero.

4 Conclusion

We have successfully prepared Pt/YSZ/LSCO mixed potential sensors by AM and assessed their sensitivity to NO_x, C_3H_8, and NH_3. The current bias effectiveness and signal magnitude were diminished in the absence of an insulating protective layer to isolate the electrodes from the substrate. Variability within the batch of sensors was studied using impedance spectroscopy, and the gas reactions impedance (R4) was found to be a useful quality control parameter to predict the signal response. The surface area of Pt and the effective diffusion coefficient

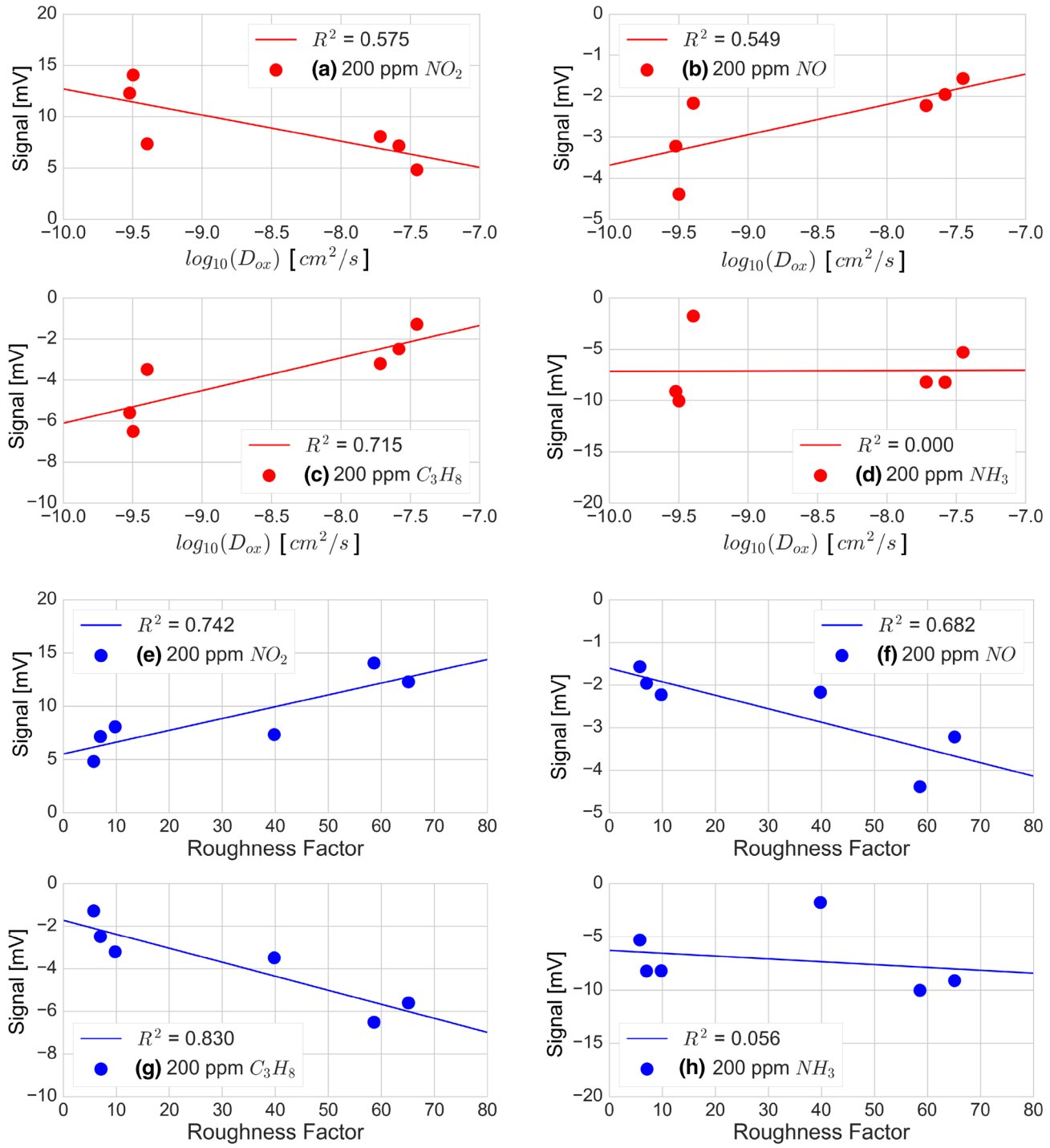

Fig. 7 Increased signal magnitude is observed for NO_x and C_3H_8 with the **a–d** a decrease in the log of the diffusion coefficient for $Fe(CN)_6^{3+}$ oxidation and **d, e** an increase in the roughness factor of the Pt electrodes

through the porous YSZ electrolyte were correlated to signal response, and mechanisms involving heterogeneous catalysis of the electrolyte and electrode components as well as the influence of diffusion limiting current on the difference in mixed potential of the two electrodes were proposed.

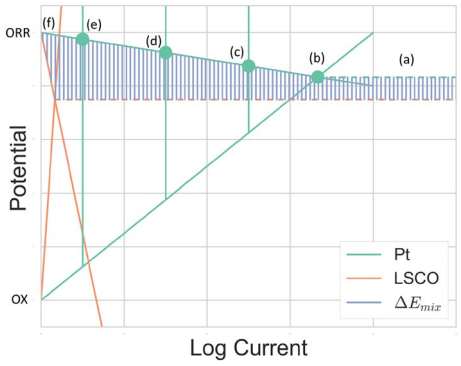

Fig. 8 A qualitative schematic of the mixed potential system showing a region where a decrease in diffusion coefficient results in a increase in the difference between the mixed potential of the two electrodes. **a** Neither electrode is under kinetic control and the difference in mixed potential is independent of diffusion. **b–e** The mixed potential of Pt is determined by the interception of the diffusion limiting current of OX with ORR while the mixed potential of LSCO is fixed under kinetic control. In this region slower diffusion implies a larger difference in mixed potential. **f** Both electrodes are under diffusion control and the difference tends towards zero

Acknowledgements We acknowledge funding from the University of New Mexico Center for Micro-Engineered Materials and the Sandia National Laboratories LDRD program through funding code DE-AC04-94-AL85000.

Compliance with ethical standards

Conflict of interest The authors declare that they have no conflict of interest.

References

1. Travitzky N, Bonet A, Dermeik B, Fey T, Filbert-Demut I, Schlier L, Schlordt T, Greil P (2014) Additive manufacturing of ceramic-based materials. Adv Eng Mater 16:729–754. https://doi.org/10.1002/adem.201400097
2. Lenk R (2000) Rapid Prototyping of ceramic components. Adv Eng Mater 2:40–47. https://doi.org/10.1002/(Sici)1527-2648(200002)2:1/2<40::Aid-Adem40>3.0.Co;2-Z
3. Allahverdi M, Danforth SC, Jafari M, Safari A (2001) Processing of advanced electroceramic components by fused deposition technique. J Eur Ceram Soc 21:1485–1490. https://doi.org/10.1016/S0955-2219(01)00047-4
4. Sarobol P, Cook A, Clem PG, Keicher D, Hirschfeld D, Hall AC, Bell NS (2016) Additive manufacturing of hybrid circuits. Annu Rev Mater Res 46:41–62. https://doi.org/10.1146/annurev-matsci-070115-031632
5. Cesarano J (2011) A review of robocasting technology. MRS Proc 542:133–139. https://doi.org/10.1557/PROC-542-133
6. Ibrahim H, Jahadakbar A, Dehghan A, Moghaddam NS, Amerinatanzi A, Elahinia M (2018) In vitro corrosion assessment of additively manufactured porous NiTi structures for bone fixation applications. Metals. https://doi.org/10.3390/met8030164
7. Trevisan F, Calignano F, Aversa A, Marchese G, Lombardi M, Biamino S, Ugues D, Manfredi D (2017) Additive manufacturing of titanium alloys in the biomedical field: processes, properties and applications. J Appl Biomater Funct Mater 16:57–67. https://doi.org/10.5301/jabfm.5000371
8. Cuellar JS, Smit G, Plettenburg D, Zadpoor A (2018) Additive manufacturing of non-assembly mechanisms. Addit Manuf 21:150–158. https://doi.org/10.1016/j.addma.2018.02.004
9. Lehmhus D, Busse M (2017) Sensor and electronics integration in additive manufacturing. In: Material-integrated intelligent systems—technology and applications. Wiley, Weinheim, pp 217–256
10. Ngo TD, Kashani A, Imbalzano G, Nguyen KTQ, Hui D (2018) Additive manufacturing (3D printing): a review of materials, methods, applications and challenges. Compos Part B Eng 143:172–196. https://doi.org/10.1016/j.compositesb.2018.02.012
11. Chang JB, Liu V, Subramanian V, Sivula K, Luscombe C, Murphy A, Liu J, Fréchet JMJ (2006) Printable polythiophene gas sensor array for low-cost electronic noses. J Appl Phys. https://doi.org/10.1063/1.2208743
12. Swerin A, Mira I (2014) Ink-jettable paper-based sensor for charged macromolecules and surfactants. Sens Actuators B Chem 195:389–395. https://doi.org/10.1016/j.snb.2014.01.064
13. Sarfraz J, Ihalainen P, Määttänen A, Gulin T, Koskela J, Wilén CE, Kilpelä A, Peltonen J (2014) A printed H2S sensor with electro-optical response. Sens Actuators B Chem 191:821–827. https://doi.org/10.1016/j.snb.2013.10.011
14. Fergus JW (2011) Sensing mechanism of non-equilibrium solid-electrolyte-based chemical sensors. J Solid State Electrochem 15:971–984. https://doi.org/10.1007/s10008-010-1046-4
15. Garzon FH, Mukundan R, Brosha EL (2000) Solid-state mixed potential gas sensors: theory, experiments and challenges. Solid State Ionics 136–137:633–638. https://doi.org/10.1016/S0167-2738(00)00348-9
16. Kreller CR, Spernjak D, Li W, Palanisamy P, Brosha EL, Mukundan R, Garzon F (2014) Mixed-potential NO_x and NH_3 sensors fabricated by commercial manufacturing methods. ECS Trans 64:105–113. https://doi.org/10.1149/06401.0105ecst
17. Tsui L, Benavidez A, Palanisamy P, Evans L, Garzon F (2017) Quantitative decoding of the response a ceramic mixed potential sensor array for engine emissions control and diagnostics. Sens Actuators B Chem 249:673–684. https://doi.org/10.1016/j.snb.2017.04.060
18. Kreller CR, Sekhar PK, Prikhodko V, Pihl J, Curran S, Parks JE, Mukundan R, Garzon F, Brosha EL (2014) Dynamometer testing of planar mixed-potential sensors. ECS Trans 61:55–63. https://doi.org/10.1149/06119.0055ecst
19. Sekhar PK, Brosha EL, Mukundan R, Li W, Nelson MA, Palanisamy P, Garzon FH (2010) Application of commercial automotive sensor manufacturing methods for NO_x/NH_3 mixed potential sensors for on-board emissions control. Sens Actuators B Chem 144:112–119. https://doi.org/10.1016/j.snb.2009.10.045
20. Sekhar PK, Mukundan R, Brosha E, Garzon F (2013) Effect of perovskite electrode composition on mixed potential sensor response. Sens Actuators B Chem 183:20–24. https://doi.org/10.1016/j.snb.2013.03.110
21. Fergus JW (2007) Solid electrolyte based sensors for the measurement of CO and hydrocarbon gases. Sens Actuators B Chem 122:683–693. https://doi.org/10.1016/j.snb.2006.06.024
22. Tsui L, Benavidez AD, Palanisamy P, Evans L, Garzon FH (2016) A three electrode mixed potential sensor for gas detection and discrimination. ECS Trans 75:9–22. https://doi.org/10.1149/07516.0009ecst
23. Tsui L, Benavidez AD, Evans L, Garzon FH (2017) Characterization of electrochemical surface area and porosity of zirconia

sensors. ECS Trans 77:1087–1094. https://doi.org/10.1149/07711.1087ecst
24. Kilner JA, Steele BCH (1981) Nonstoichiometric oxides. Elsevier, Amsterdam
25. Pajkossy T, Kolb DM (2001) Double layer capacitance of Pt(111) single crystal electrodes. Electrochim Acta 46:3063–3071. https://doi.org/10.1016/S0013-4686(01)00597-7
26. Hamann CH, Hamnett A, Vielstich W (1998) Methods for the study of the electrode/electrolyte interface. In: Electrochemistry. Wiley, Weinheim, pp 236–247
27. Tuller H (2000) Ionic conduction in nanocrystalline materials. Solid State Ionics 131:143–157. https://doi.org/10.1016/S0167-2738(00)00629-9